ACS Catalysis

Research Article

pubs.acs.org/acscatalysis

Uncoupled Epimerization and Desaturation by Carbapenem Synthase: Mechanistic Insights from QM/MM Studies

Guangcai Ma, Wenyou Zhu, Hao Su, Na Cheng, and Yongjun Liu*

Key Laboratory of Colloid and Interface Chemistry, Ministry of Education, School of Chemistry and Chemical Engineering, Shandong University, Jinan, Shandong 250100, China

Supporting Information

ABSTRACT: Author: Carbapenem antibiotics possess a broad spectrum of antibacterial activity and high resistance to hydrolytic inactivation by *β*-lactamases. Carbapenem synthase (CarC), an iron(II) and 2-(oxo)glutarate-dependent oxygenase, catalyzes the epimerization and desaturation of (3*S*,5*S*)-carbapenam to produce (5*R*)-carbapenem in the last step of the simple carbapenem biosynthesis. Recently, the complete crystal structure of CarC was reported, allowing us to perform accurate quantum mechanics/molecular mechanics calculations to explore the detailed reaction mechanism. We first analyzed the dioxygen binding site on metal and identified that the Fe^{IV}−oxo species has two potential orientations with the oxo group trans to either His101 or His251. The former is energetically unstable, which can rapidly isomerize into the latter by rotation of the oxo group. Arg279 plays important roles in regulating the dioxygen binding and assisting the isomerization of Fe^{IV}−oxo species. The calculation results clearly support the stepwise C5-epimerization and C2/3-desaturation processes, involving two complete oxidative cycles. The epimerization process converts (3*S*,5*S*)-carbapenam to the initial product (3*S*,5*R*)-carbapenam, undergoing H5 atom abstraction by $Fe^{IV}{=}O$ species, inversion of the C5-radical, and reconstitution of the inverted C5−H bond by Tyr165. In the desaturation process, (3*S*,5*R*)-carbapenam rebinds the CarC active site with a new orientation different from what (3*S*,5*S*)-carbapenam does in the epimerization. In addition, the desaturation across C2−C3 occurs without involving any active site residue other than the $Fe^{IV}{=}O$ center. Whereas Tyr165 is not involved in the desaturation reaction, it plays a key role in binding (3*S*,5*R*)-carbapenam. (3*S*,5*R*)-Carbapenam is a substrate superior to its epimer (3*S*,5*S*)-carbapenam for CarC to produce (5*R*)-carbapenem by efficient desaturation. In addition, the substrate hydroxylations compete with the target epimerization and desaturation reaction.

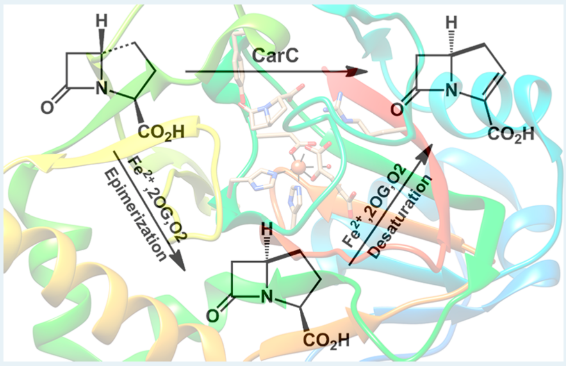

KEYWORDS: *carbapenem synthase, QM/MM, dioxygen binding, epimerization, desaturation*

1. INTRODUCTION

Carbapenems, one subclass of *β*-lactam antibiotics, have been widely used in human medicine in the past decade. They retain a broad spectrum of antibacterial activity and remarkable potency against both Gram-positive and Gram-negative bacteria.[1] The carbapenem members, such as panipenem,[2] Meropenem,[3] ertapenem,[4] and doripenem,[5] possess high resistance to many serine *β*-lactamases that usually deactivate the *β*-lactam antibiotics by hydrolyzing the lactam rings.[6−8] However, recent studies clearly showed that the bacterial resistance to carbapenems is increasing.[9−12] A complete understanding of the biosynthesis of carbapenem, thus, is critically important for designing new drug variants to combat resistance.

Biosynthetic studies of carbapenems have been extensively conducted since thienamycin, one member of carbapenems, was first isolated from *Streptomyces cattleya*.[13] Earlier biochemical studies identified three distinct enzymes, including carbapenam synthetase (CarA), carboxymethylproline synthase (CarB), and carbapenem synthase (CarC), sufficiently required for the biosynthesis of the simplest natural carbapenem, carbapenem-3-carboxylic acid (**3**), in the phylogenetically distant plant pathogen *Pectobacterium carotovorum*.[14−16] Moreover, Bodner et al. found that the biosynthetic pathway to **3** shares the first two steps catalyzed by CarB and CarA with thienamycin (ThnE and ThnM in *S. cattleya*) but diverges from the third step.[17]

On the basis of amino acid sequence analysis, CarC has been characterized as a member of iron(II) and 2-(oxo)glutarate (Fe/2OG)-dependent oxygenases.[14,18] These oxygenases commonly exhibit a His-Asp/Glu-His facial-triad iron(II)-binding motif, which leaves three remaining sites on the metal available to coordinate the cosubstrate 2OG and molecular oxygen.[19,20] After 2OG and dioxygen binding, the formed iron(III)−superoxo species reacts with 2OG to generate succinate (Succ), CO_2, and a high-valent iron(IV)−oxo ($Fe^{IV}{=}O$) intermedi-

Received: June 17, 2015
Revised: August 16, 2015
Published: August 18, 2015

DOI: 10.1021/acscatal.5b01275
ACS Catal. 2015, 5, 5556−5566

ate.[21,22] This iron(IV)−oxo intermediate is a highly reactive species and has been characterized by spectroscopic experiments in some nonheme iron dioxygenases[23] that usually functionalize unactivated C−H bonds selectively.[24,25] CarC catalyzes the epimerization of (3*S*,5*S*)-carbapenam **1** to the initial product (3*S*,5*R*)-carbapenam **2** and then desaturates it across the C2−C3 bond to produce (5*R*)-carbapenem **3** (Figure 1).[14,26]

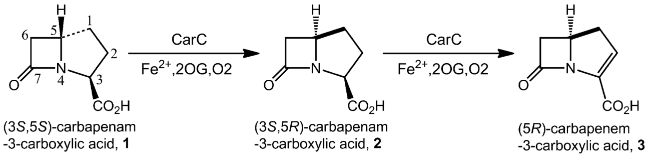

Figure 1. C5-Epimerization and C2/3-desaturation catalyzed by CarC.

Clifton et al. reported the first crystal structure of CarC in the presence of substrate analogue.[18] However, two loop segments surrounding the active site in this protein, which is supposed to be responsible for closing or opening the active site, were missed. On the basis of this crystal structure, a radical epimerization mechanism was proposed from both experiments and theoretical calculations in which the hybrid density functional method B3LYP and the simple active site model were employed. Specifically, the reactive iron(IV)−oxo species abstracts H· of carbapenam **1** to give a C5-based radical, and subsequently, a CarC active site tyrosine (Tyr67) functions as a radical donor to donate a H· to the opposite face of the substrate radical to form **2**, Fe^{III}−OH, and a tyrosyl radical.[27−29] Given the imperfection of the initially reported structure, the results of these studies appear to be suspect.

Recently, Chang et al. reported a complete crystal structure of CarC in complex with substrate, iron(II), and 2OG with a resolution of 2.10 Å (PDB code: 4OJ8).[30] Structural analysis of CarC revealed that Tyr165, rather than Tyr67 that locates at the edge of the active pocket, is the preferred H· donor, and mutational studies further confirmed its crucial importance for catalysis.[30] Experimental studies by the Townsend group have revealed that both **1** and the bridgehead-inverted **2** can act as a substrate of CarC.[28] If the substrate is **2**, CarC can directly desaturate it to produce the final (5*R*)-carbapenem product. In the desaturation process, based on the earlier reported incomplete crystal structure, the docking studies further suggested that the (3*S*,5*R*)-carbapenam intermediate adopts a new orientation in the CarC active site, which is remarkably different from what the (3*S*,5*S*)-carbapenam does in the epimerization process. Furthermore, they proposed that, after completion of epimerization, CarC prefers to undergo a second round of O_2 activation and $Fe^{IV}{=}O$ formation, rather than continuing to utilize the Fe^{III}−OH and tyrosyl radical generated in the epimerization step to complete the ultimate C2−C3 desaturation.[28]

Inspection of the recently reported CarC structure reveals that the coordination position trans to His101 is occupied by a water molecule (Figure 2). By analogy with some nonheme dioxygenases, such as factor inhibiting HIF[31] and clavaminate synthase,[32] the dioxygen seems to substitute for the water ligand to bind Fe^{II} ion to form a Fe^{III}−superoxo complex. As such, the oxo group of $Fe^{IV}{=}O$ species obtained from the oxidative decarboxylation of 2OG is supposed to occupy this site, which is far from the substrate (the distance between the oxo and the C5 atom of the substrate is close to 6 Å).

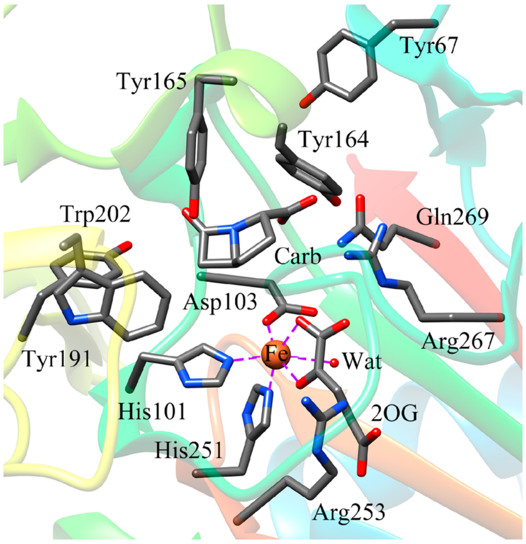

Figure 2. Active site of CarC in complex with substrate (3*S*,5*S*)-carbapenam (Carb), iron(II), and cosubstrate 2-(oxo)glutarate (2OG) (PDB code: 4OJ8).

Furthermore, previous DFT studies of the mechanism of CarC by the Siegbahn group used simple cluster models and did not consider the real protein environment.[29] Calculation results supported the CarC-catalyzed coupled epimerization/desaturation mechanism proposed by Topf et al.[33] which, however, is inconsistent with the recent experimental proposal.[28,30]

Here, we report the first quantum mechanical/molecular mechanical (QM/MM) calculations to uncover the reaction mechanism of CarC. In recent years, the QM/MM method has been extensively and successfully applied to elucidate the nature of reaction mechanisms of iron-containing enzymes, such as cytochrome P450 enzyme[34,35] and nonheme iron dioxygenases.[36−38] In this work, based on the recently reported crystal structure and our QM/MM calculations, we clearly identify the dioxygen binding site on the metal and the orientation of the iron(IV)-oxo species, and further propose the detailed C5-epimerization and C2/3-desaturation mechanisms. In addition, our calculation results support the stepwise epimerization and desaturation reactions.

2. COMPUTATIONAL METHODS

2.1. Setup of the System.

The initial structure of the enzyme−substrate complex was prepared on the basis of the recently reported crystal structure of CarC from *Pectobacterium carotovorum* (PDB code: 4OJ8).[30] CarC functions as a trimer, and each subunit exhibits an individual active site. All the active sites are identical. Given the absence of the substrate and some key residues surrounding the active site in subunit A of the crystal structure, we chose the complete subunit B to construct the computational model. The water molecule, which coordinates to the iron(II) ion in the active site, was removed. In addition, the iron(II) and 2OG were manually modified to iron(IV)-oxo and succinate, respectively. The newly obtained iron(IV)-oxo species is a pentacoordinated complex that contains His101, Asp103, His251, and succinate.

The protonation states of all titratable residues were assigned on the basis of pK_a values measured with the PROPKA program[39] in combination with careful visual inspections by VMD software.[40] All aspartic acid and glutamic acid residues were set to their deprotonated states, and all lysine and arginine residues were protonated. Furthermore, all histidine residues were assigned in singly protonated states according to the calculated pK_a values. All missing hydrogen atoms were added to the structure by using the HBUILD facility as implemented in the CHARMM program package.[41] The system was solvated with a water sphere of radius 33 Å, and then 14 Na^+ ions were randomly added into the system to ensure the overall charge neutrality. The resulting model consisted of 16397 atoms and included 3994 TIP3P water molecules.

Before the molecular dynamics (MD) simulation, the solvated system was first subjected to a series of energy minimizations. Subsequently, the system was slowly heated from 0 to 300 K for 200 ps with a 1 fs time step, and then followed by 200 ps of equilibration at 300 K with a 1 fs time step. To attain equilibrium of the solvated model, a 15 ns MD simulation (MD-I) was performed using the CHARMM22 all-atom force field[42] with a stochastic boundary condition at 300 K and 1 bar. In MD-I, the $Fe^{IV}{=}O$, Fe-coordinated residues (His101, Asp103 and His251), succinate, and substrate were kept frozen. After that, we performed an additional 10 ns MD simulation (MD-II), in which the constraints were relaxed. From the calculated root-mean-square deviation (RMSD) of the protein structure, one can see that the system reached a basic plateau in both MD-I and MD-II (Supporting Information Figure S1). From MD-I and MD-II trajectories, a total of 12 snapshots were extracted for the following QM/MM calculations to find a relatively reasonable starting structure.

2.2. QM/MM Calculations.

All QM/MM calculations were performed using the ChemShell package,[43] which incorporates the Turbomole program[44] for the QM region and DL_POLY program[45] for the MM region. The electronic embedding scheme[46] was used to polarize the QM part by the MM point charges of the force field. No electrostatic cutoff was introduced for the MM/MM and QM/MM interactions. Hydrogen link atoms with the charge shift model[47] were applied to treat the QM/MM boundary. For geometry optimizations, the QM part was treated by the unrestricted hybrid UB3LYP[48] density functional in combination with the Wacthers+f basis set for iron and 6-31G(d,p) basis set for all other atoms, labeled BS1. On the basis of the optimized geometries, single-point energies were further calculated using the Wacthers+f and 6-31++G(d,p) basis sets combination (BS2).[49,50] The MM part was described at the CHARMM22 force field through the DL_POLY program.

Unless noted otherwise, the QM region contained the $Fe^{IV}{=}O$ unit, 2-His-1-Glu facial triad (His 101, His251 and Asp103), Tyr165, Arg267, succinate (Succ), and substrate carbapenem-3-carboxylic acid (Carb) with a total charge of −1, as shown in Figure 3. The remaining atoms of the solvated model were assigned to the MM part. We defined an active region within 13 Å of the iron atom of the $Fe^{IV}{=}O$ unit, including the QM region and partial MM atoms. The active region was fully optimized, whereas the remaining MM atoms were kept frozen. Geometry optimizations were performed with the hybrid delocalized internal coordinates (HDLC) optimizer,[51] combining the quasi-Newton limited memory Broyden−Fletcher−Goldfarb−Shanno (L-BFGS) method[52,53] for locating minima and the partitioned rational function optimization (P-RFO) algorithm[54] for transition state searches.

2.3. Empirical Dispersion Correction.

Because the B3LYP functional lacks a proper description of the attractive long-range dispersion interactions, an empirical dispersion correction was further calculated to correct the B3LYP energies using the DFT-D3 program[55] on the basis of the QM/MM-optimized geometries of the QM-region at the UB3LYP/BS1/CHHARMM22 level of theory. Previous theoretical calculations have demonstrated that the dispersion correction has an important effect on improving the accuracy of reaction barriers.[34,56] Note that the final QM/MM energies reported in the present paper are thus the single-point energies corrected for dispersion effects at the B3LYP-D/BS2// B3LYP/BS1/CHARMM22 level.

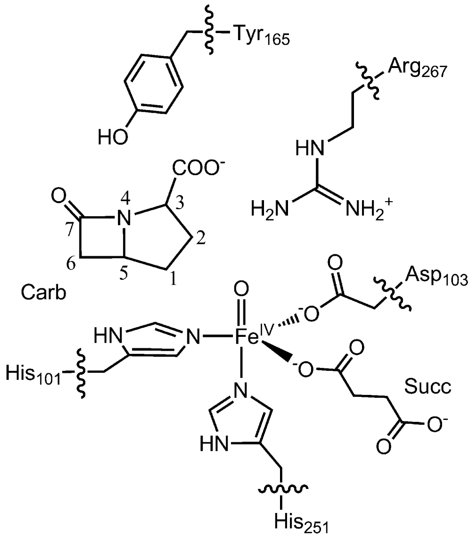

Figure 3. QM region selected for the QM/MM calculations. Carb stands for substrate, and Succ, for succinate.

3. RESULTS AND DISCUSSION

3.1. Dioxygen Binding Site.

Previous experimental and theoretical studies proposed that the CarC-catalyzed epimerization reaction starts from the high-spin Fe^{IV}−oxo species.[28−30] However, there was no relevant discussion about the dioxygen binding site on metal and the formation of the $Fe^{IV}{=}O$ unit. A close inspection of the active site structure of CarC reveals that the 2OG binds to iron(II) in a bidentate manner and the sixth coordination site of iron(II) is occupied by a water ligand. The dioxygen seems most likely to substitute for the water ligand to bind Fe^{II}, forming a Fe^{III}−superoxo complex. One might expect that the reaction between Fe^{III}−superoxo and 2OG will lead to the formation of Fe^{IV}−oxo species with the oxo group trans to His101, which is located at an incorrect orientation relative to the substrate. This disagrees with the early theoretical proposal that the oxo group is aligned with the substrate (trans to His251).[29]

Here, on the basis of the crystal structure, we constructed two models to investigate the dioxygen binding site on metal as well as the activation reaction, as shown in Figure 4. The dioxygen can directly replace the water ligand to bind the Fe^{II} ion (model A). Alternatively, the carboxylate and carbonyl groups of 2OG coordinated to iron first extrude the water ligand by a rotation of about 90°, leaving an empty binding site on metal. The dioxygen subsequently enters the empty site to form the Fe^{III}−superoxo species (model B). Structural analysis suggests that both models A and B are stereochemically feasible, and their binding pockets have enough space to accommodate the dioxygen. Figure 5 shows the QM/MM-optimized geometries of the two models. One can see that the side chain of Arg267 is located within hydrogen bonding

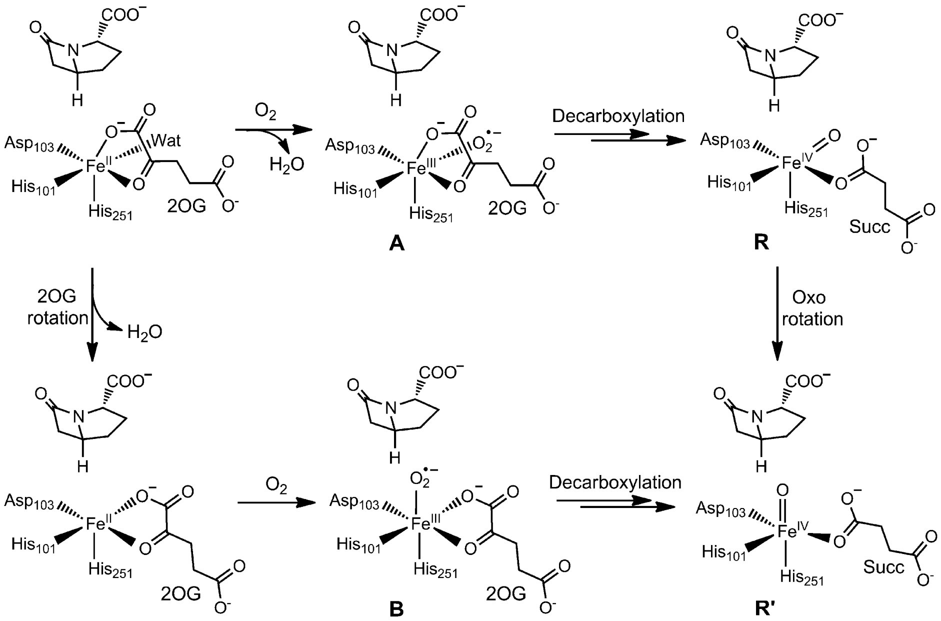

Figure 4. Possible dioxygen binding and activation in carbapenem synthase.

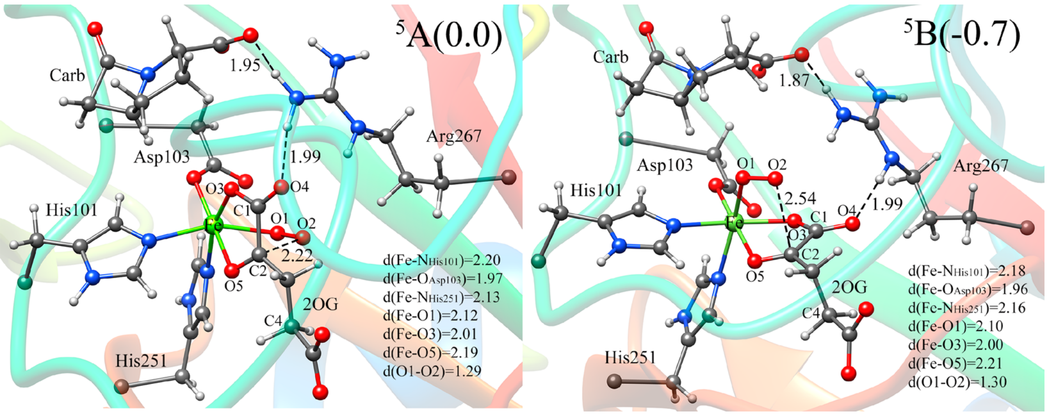

Figure 5. QM/MM-optimized geometries for dioxygen binding to the iron(II) center of CarC with the O_2 either trans to His101 (model A) or trans to His251 (model B). Note that the QM part includes iron(II), molecular oxygen, 2-His-1-Glu facial triad (His 101, His251, and Asp103), Arg267, 2OG, and the substrate. All distances are shown in angstroms. Relative energies (kcal/mol) are given in parentheses.

distances to the substrate and 2OG in both models A and B, which is thought to play an important role in regulating the dioxygen binding. In model A, the d(O2−C2) is 2.22 Å, whereas it is 2.54 Å in model B, which suggests that model A seems to be more favorable for the oxidative decarboxylation reaction of 2OG by the Fe^{III}−superoxo complex to form the Fe^{IV}=O species. Intriguingly, the Fe^{IV}=O species formed in model A positions its oxo group trans to His101 (R), which is incapable of reacting with the substrate owing to its incorrect orientation. In contrast, the Fe^{IV}=O species obtained from model B puts its oxo group trans to His251 (R′), which can directly abstract the hydrogen atom of the substrate, although the formation of Fe^{IV}=O involves more complex steps than model A. The relative energy of model A is calculated to be only 0.7 kcal/mol higher than that of model B, indicating the coexistence of the two structures.

Taken together, models A and B are thermodynamically and structurally favorable; in other words, there are two possible positions for molecular oxygen to bind the iron(II) center with the superoxo group: either trans to His101 or trans to His251. Thus, the Fe^{IV}=O species obtained from the dioxygen activation reaction has two potential orientations, with the oxo group either trans to His101 or trans to His251. Although the Fe^{IV}=O species formed in model A deviates from the substrate, it is still possible to start up the hydrogen atom abstraction reaction by an oxo rotation from trans to His101 to trans to His251, which is supported by the computational precedents of AlkB and SyrB2 enzymes.[37,57] The isomerization reaction of Fe^{IV}=O species will be discussed in Section 3.3.

3.2. Selection of Reactant Complex ^{5}R′.

Previous QM/MM studies of some enzymatic reactions have revealed that the selection of initial geometries significantly affects the accuracy of the calculation results.[58−60] To explore the reaction pathway, we extracted a series of snapshots from the MD trajectories as the starting structures for the QM/MM calculations. In MD-I, six snapshots were extracted at an interval of 200 ps from 14 to 15 ns, which were designated as models M1−M6. In addition, we chose another six snapshots from MD-II at an interval of 200 ps from 5 to 6 ns, which were designated as models M7−M12. The superposition of these 12 QM/MM optimized reactant complexes ^{5}R′s (Figure S2) shows only a little difference in the CarC active site, which is thought to be

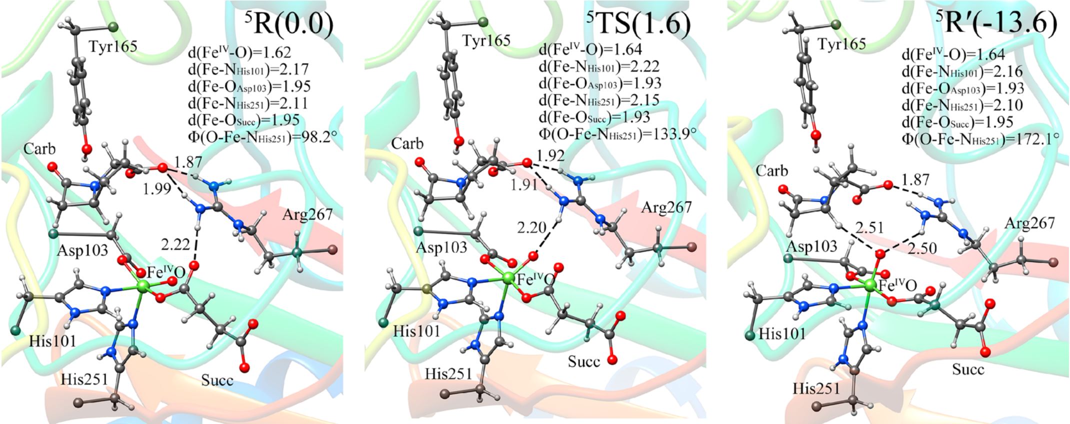

Figure 6. QM/MM-optimized quintet state structures of reactant complexes (^{5}R and ^{5}R′) and transition state ^{5}TS for the isomerization of Fe^{IV}−oxo species. Relative energies (kcal/mol) are given in parentheses. All distances are shown in angstroms; angles, in degrees.

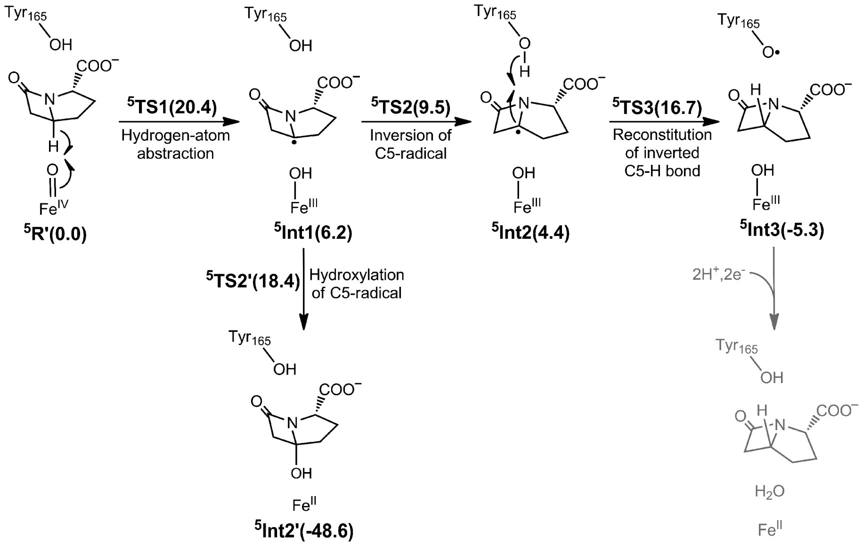

Figure 7. Competitive epimerization and hydroxylation mechanisms of CarC based on the QM/MM calculations. Relative energies (kcal/mol) on quintet spin state surface are given in parentheses.

inevitable during the MD simulation. The major conformational variability among the 12 models is found on the surface of the protein, which is far from the CarC reaction center. As will be demonstrated later, the epimerization reaction of CarC shows a quintet spin ground state and a rate-limiting hydrogen atom abstraction step. Consequently, we focus on only the hydrogen atom abstraction step for these 12 models to find a relatively reasonable reaction path. On the basis of the optimized ^{5}R′s, we scanned the potential energy surfaces of the hydrogen atom abstraction step along the reaction coordinates with a small increment of 0.04 Å. The vertexes of the potential energy surface were regarded as the approximate hydrogen atom abstraction transition states (^{5}TS1s).

Table S1 summarizes some key distances in the active sites and the scanned hydrogen atom abstraction barriers of these 12 models. Comparison of these models reveals slight differences of two Fe−N distances with His101 and His251 and two Fe−O distances with Asp103 and succinate. The model M5 shows a shorter distance between the hydrogen atom at C5 of the substrate and the oxygen atom of Fe^{IV}−oxo and smaller barrier than those of the other models, meaning that model M5 should be the preferred structure for exploring the CarC-catalyzed reaction process. Note that all the subsequent QM/MM calculations were based on model M5.

3.3. Isomerization of Fe^{IV}−Oxo Species.

As aforementioned, the orientation of the Fe^{IV}═O species in structure R strictly restricts the hydrogen atom abstraction of CarC compared with R′. Previous QM/MM studies of AlkB repair enzyme by the De Visser group suggested an initial isomerization of the Fe^{IV}-oxo unit, which brings the oxo group closer to the substrate and thereby enables the following hydrogen atom abstraction from substrate.[37] Here, we explored the rotation of the oxo group from a position trans to His101 to trans to His251 (see Figure 4). Figure 6 displays the optimized quintet spin state structures of reactant complexes (^{5}R and ^{5}R′) and transition state ^{5}TS for the isomerization reaction. In structure ^{5}R, Arg267 lies within hydrogen bonding distance to substrate and succinate, and the bond length of Fe^{IV}═O is 1.62 Å, with the oxo group trans to His101. Along the oxo rotation, the bond angle of O−Fe−N$_{His251}$ changes from 98.2° in ^{5}R to 133.9° in ^{5}TS and, finally, to 172.1° in ^{5}R′. The spin population on the metal is slightly increased from 3.06 in ^{5}R to 3.15 in ^{5}R′. Meanwhile, the oxo group reduces the spin population from 0.73 in ^{5}R to 0.69 in ^{5}R′ (see Table S2). In ^{5}TS, two Fe−N distances with His101 and His251 are slightly elongated as a result of the hydrogen bonding interaction between Arg267 and the oxo group with a distance of 2.20 Å, which is elongated to 2.50 Å in ^{5}R′. In addition, structural comparison of ^{5}R, ^{5}TS, and ^{5}R′ suggests that Arg267 plays an important role in assisting the isomerization of Fe^{IV}−oxo species and stabilizing the generated transition state.

According to the QM/MM calculations, the oxo group of the Fe^{IV}−oxo species in ^{5}R rotates via a low barrier (1.6 kcal/mol) process to form the energetically more stable structure ^{5}R′. This implies that the isomerization of Fe^{IV}−oxo species in the active site is a quite rapid process. Note that the QM/MM model used for the study of the epimerization mechanism of CarC was created from the structure R′, rather than R.

3.4. Epimerization Mechanism.

According to the QM/MM calculations, we have suggested a complete epimerization mechanism of CarC, as shown in Figure 7. The oxo group of Fe^{IV}−oxo species first abstracts the C5−H of the substrate to generate a C5-radical intermediate (Int1), then the C5-radical undergoes an inversion to form an intermediate Int2, which is stereochemically favorable to abstract the hydrogen atom from Tyr165 to reconstruct the inverted C5−H bond (Int3).

Despite the fact that the ferryl complex can exist in either quintet or triplet ground states, previous theoretical studies have suggested that the quintet iron(IV)−oxo species exhibits higher reactivity than the other spin states.[37,61,62] For the optimized enzyme−substrate complex (R′) of CarC, the quintet spin state is calculated to be the ground state, and the energy increases in the order: quintet < triplet < septet < singlet (Figure S3), which is in agreement with the QM/MM studies of AlkB repair enzyme by Quesne et al.[37] Therefore, we calculated only the triplet and quintet spin state surfaces for the CarC-catalyzed epimerization process, and the discussion focuses mainly on the quintet spin state surface. The energy profiles on the quintet and triplet spin state surfaces along the reaction path are shown in Figure S5, and the optimized quintet and triplet spin state geometries of all the structures are shown in Figures S6 and S7, respectively.

3.4.1. Hydrogen Atom Abstraction.

Previous studies have revealed that the hydrogen atom abstraction reaction proceeds through two possible channels on the quintet spin state surface.[61,63−65] One is $^5\sigma$-channel, in which an α electron is transferred from the substrate to the Fe−O σ^* orbital with an Fe−O−H angle of 180°. Alternatively, a β electron is transferred from the substrate to the Fe−O π^* orbital with an Fe−O−H angle of 120°. This is a $^5\pi$-channel.[61,63−65] Compared with the $^5\sigma$-channel, the $^5\pi$-channel usually shows a higher energy barrier because of the stereochemically disfavored interaction.[37,66,67]

TS1 corresponds to the hydrogen atom abstraction transition state. In ^{5}TS1, the distance of d(H5−O) is shortened to 1.23 Å, and simultaneously, the O−Fe bond elongates from 1.64 Å in ^{5}R′ to 1.77 Å in ^{5}TS1 and finally, to 1.83 Å in ^{5}Int1. Structural analysis of ^{5}R′ reveals that the oxo group is in close proximity to the C5−H5 of the substrate, with a distance of 2.51 Å, and the Fe−O−H angle is 104.9°, which is slightly smaller than the ideal angle of 120°. During the hydrogen atom abstraction, a β electron is transferred into the low-lying Fe π^*_{xy} orbital, forming the intermediate ^{5}Int1 with $\pi^{*2}_{xy}\ \pi^{*\uparrow}_{xz}\ \pi^{*\uparrow}_{yz}\ \sigma^{*\uparrow}_{x^2-y^2}$ $\sigma_{sub}^{\uparrow}$ configuration (Figure S4). As such, the H5 atom transfer occurs via the $^5\pi$-channel. However, the long distance of d(O−H5) and unfavorable angle undeniably result in poor orbital overlap between the Fe−O and C5−H5 bonds, thereby causing a relatively high hydrogen abstraction barrier (20.4 kcal/mol in Figure 7), which indicates that the hydrogen atom abstraction is the rate-limiting step of the epimerization reaction. The spin populations on C5, Fe, and O atoms exhibit significant changes during the hydrogen atom abstraction, which should be indicative of the formation of C5-radical and Fe^{III}−OH species. Compared with ^{5}R′, the formed intermediate ^{5}Int1 is intrinsically unstable because of the existence of C5-radical.

3.4.2. Inversion of C5-Radical.

On the basis of the early reported crystal structure (PDB code: 1NX8), Borowski and Phelan et al. proposed that Tyr67 donates a hydrogen atom to the C5-radical to accomplish the bicyclic ring inversion.[28,29] However, structural analysis of recently reported crystal structure reveals that Tyr67 is located at the edge of the active pocket.[30] Actually, the mutational data together with our QM/MM calculations strongly confirm the vital importance of Tyr165 for catalysis; that is, Tyr165 is the sole hydrogen atom donor.

In ^{5}Int1, the distance between the C5 and hydrogen atom of phenolic hydroxyl of Tyr165 is 3.67 Å, and at the same time, the C5 positions its radical away from Tyr165, which are the disadvantages of reconstitution of inverted C5−H bond. Accordingly, the previous proposal[28,30] that tyrosine donates a hydrogen atom to the opposite face of the C5-radical is actually unrealistic. Our QM/MM calculations demonstrate that after the hydrogen atom abstraction, the C5-radical undergoes an inversion at the radical center, forming intermediate ^{5}Int2. The calculated barrier is 3.3 kcal/mol relative to ^{5}Int1, suggesting the inversion step to be a facile process.

In ^{5}TS2, the central part of the fused rings of substrate is almost planar, with a C7−N4−C5−C1 dihedral angle of 170.0°, and the distance of C5−H$_{Tyr165}$ is shortened to 2.77 Å and is further shortened to 2.10 Å in ^{5}Int2. Comparison of ^{5}Int1 and ^{5}Int2 reveals that the spin populations and bond lengths experience only slight changes during the inversion reaction.

3.4.3. Reconstitution of Inverted C5−H Bond.

Structural analysis of ^{5}Int2 reveals that the C5-radical is located at an ideal position to abstract the hydrogen atom of Tyr165 to reconstruct the inverted C5−H bond. The barrier of hydrogen transfer is calculated to be 12.3 kcal/mol relative to ^{5}Int2.

The hydrogen transfer leads to the formation of intermediate (3*S*,5*R*)-carbapenam (Int3), Fe^{III}−OH, and Tyr165·, which has been confirmed by experiments.[30] The whole epimerization reaction is exothermic by 5.3 kcal/mol, and the ^{5}Int3 is stereochemically and energetically more stable than the reactant complex ^{5}R′. It should be noted that, along the reaction coordinate, Arg267 is located within hydrogen bonding distance to the carboxyl group of the substrate and the formed Fe^{III}−OH species.

We also explored the hydroxyl group rebound from the Fe^{III}−OH species to C5-radical. The hydroxyl rebound leads to the regeneration of the ferrous resting state of the enzyme and the formation of the byproduct (3*S*,5*R*)-5-hydroxylcarbapenam (Int2′). Energetically, although the generated ^{5}Int2′ is more stable than ^{5}Int2, the OH rebound barrier is much higher than the inversion barrier (12.2 vs 3.3 kcal/mol relative to ^{5}Int1). This implies that the C5-radical kinetically prefers to undergo an inversion rather than accept the OH to form the ^{5}Int2′. Considering the relatively high barrier of C5−H bond reconstitution, the substrate hydroxylation is still competitive with the target epimerization. It can be speculated that the mutation of Tyr165 into Phe will entirely hamper the reconstitution of inverted C5−H bond, but the energetically favorable formation of ^{5}Int2′ is inevitable, which can well elucidate the catalytic consumption of substrate in the Tyr165Phe variant.[30]

3.5. Desaturation Mechanism. Desaturation is a common reaction catalyzed by both Fe(II)/2OG-dependent dioxygenase and cytochrome P450 enzyme.[25,68] Because of the protein instability and product lability, the crystal structures of CarC in complex with either intermediate (3*S*,5*R*)-carbapenam or product (5*R*)-carbapenem have not been reported yet, which thwarts the mechanistic studies of the CarC-catalyzed desaturation process. Early mechanistic studies of the desaturation reaction of CarC have proposed that the generated $\mathrm{Fe^{III}{-}OH}$ species and tyrosyl radical in the epimerization directly take part in the ultimate C2−C3 desaturation; thereby, the tyrosyl radical removes the hydrogen atom from C3, and subsequently, the $\mathrm{Fe^{III}{-}OH}$ species abstracts the hydrogen atom from C2 to form the desaturated (5*R*)-carbapenem.[29] However, recent experimental observations have supported the stepwise C5-epimerization and C2−C3 desaturation, involving two separate oxidative cycles.[28,30] After completion of the epimerization process, it has been proposed that the tyrosine radical is reductively quenched, and the CarC rebinds the 2OG, intermediate (3*S*,5*R*)-carbapenam, and dioxygen to carry out the C2−C3 desaturation reaction.[28]

Figure 8 shows the QM/MM-optimized geometry of ^{5}Int3. It is found that Tyr165 radical and the hydroxyl group of $\mathrm{Fe^{III}}$−OH species are located at unfavorable positions to abstract the hydrogen atoms from C3 and C2, respectively (both $d(\mathrm{O_{Tyr165}}$-H3) and d(O−H21) are close to 5 Å). It is well established that the enzymatic reaction is highly sensitive to the proper conformation and orientation of the substrate. However, since the ^{5}Int3 is much more stable than ^{5}R′, it may have sufficient time to relax the conformation and orientation of the (3*S*,5*R*)-carbapenam intermediate. Bearing this in mind, on the basis of the optimized geometry of ^{5}Int3, we performed an additional 15 ns MD run (MD-III) to explore the change of conformation and orientation of (3*S*,5*R*)-carbapenam in the CarC active site.

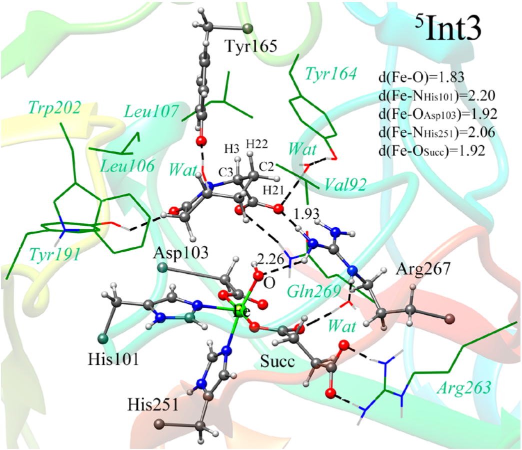

Figure 8. QM/MM-optimized quintet spin state geometry of ^{5}Int3. QM part is shown in ball-and-stick representation. All distances are in angstroms.

According to our MD simulation result, the (3*S*,5*R*)-carbapenam dynamically adjusts the orientation of C3-COO$^-$ to form a hydrogen bond with the $\mathrm{Fe^{III}{-}OH}$ species, which partially shortens the d(O−H21), but in turn elongates the $d(\mathrm{O_{Tyr165}}$−H3) (see Figure S8). We further extracted a representative snapshot from MD-III trajectories to investigate whether the Tyr165 radical is a suitable hydrogen acceptor. From the QM/MM-optimized geometry of CarC−(3*S*,5*R*)-carbapenam complex (labeled as ^{5}Int3′ to distinguish ^{5}Int3), one can see that the distances $d(\mathrm{O_{Tyr165}}$−H3) and d(O−H21) are 5.26 and 2.57 Å, respectively (Figure S9a). In both ^{5}Int3 and ^{5}Int3′, Tyr165· lies an incorrect orientation to abstract the H3 atom from the (3*S*,5*R*)-carbapenam intermediate, which results in an extremely high hydrogen-abstraction barrier (Figure S9b). This calculation result clearly demonstrates that the Tyr165· is not a suitable H3 receptor. Thus, the previously proposed coupled epimerization and desaturation reaction mechanism is essentially infeasible.

Docking studies of Phelan et al. identified two distinct orientations for substrate binding in the epimerization and desaturation processes.[28] In the desaturation process, the released bridgehead-inverted intermediate (3*S*,5*R*)-carbapenam from CarC rebinds to the active site with a new orientation.[28] In view of the docking model being created in light of the early reported incomplete crystal structure in which two key loop segments surrounding the active site have been missed, the docking result seems to be inherently speculative. Furthermore, Phelan et al. proposed an uncoupled desaturation mechanism, in which the newly formed $\mathrm{Fe^{IV}{=}O}$ species activates the C3−H3 bond of (3*S*,5*R*)-carbapenam and subsequently, the $\mathrm{Fe^{IV}{-}OH}$ species abstracts a hydrogen atom from C2, forming a water molecule, $\mathrm{Fe^{II}}$ ion, and the desaturated (5*R*)-carbapenem product (see Figure 9).[28] With these in mind, on the basis of the optimized geometry of Int3, we manually docked the (3*S*,5*R*)-carbapenam intermediate into the active site to explore the C2−C3 desaturation reaction. Given the hydrogen-bonding interactions between (3*S*,5*R*)-carbapenam and CarC active site residues, we created three models and here designate them as C, D, and E, respectively.

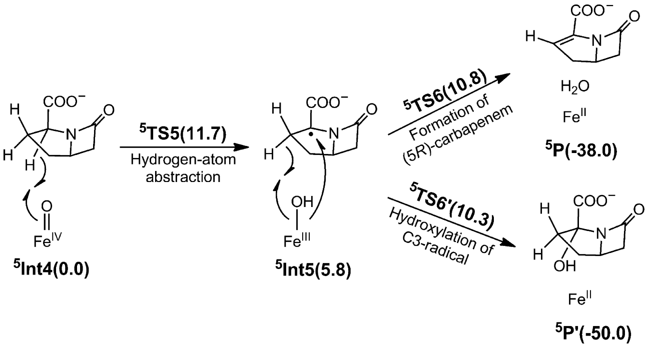

Figure 9. Competitive desaturation and hydroxylation mechanisms for (3*S*,5*R*)-carbapenam catalyzed by CarC. Relative energies (kcal/mol) on quintet spin state surface are given in parentheses.

Figure 10 shows the QM/MM-optimized geometries of models C, D, and E. Comparison among these models and ^{5}Int3 reveals apparent rotation of the (3*S*,5*R*)-carbapenam intermediate in the CarC active site, which enables the following desaturation reaction. In model ^{5}C, the (3*S*,5*R*)-carbapenam forms hydrogen bonds with the side chains of Tyr165, Tyr191, and Arg267; however, in models ^{5}D and ^{5}E, Arg267 is not located within hydrogen bonding distance to the intermediate. Previous docking results suggested that the

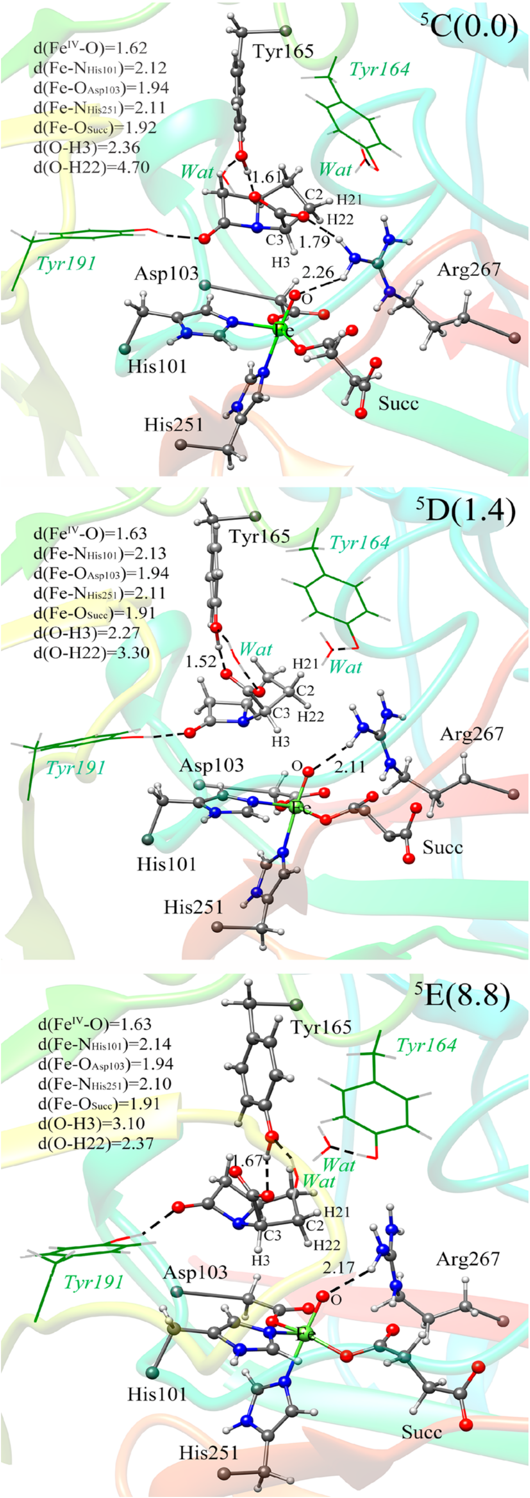

Figure 10. QM/MM-optimized geometries of models ^{5}C, ^{5}D, and ^{5}E. QM parts are shown in ball-and-stick models. Relative energies (kcal/mol) are given in parentheses. All distances are in angstroms.

(3*S*,5*R*)-carbapenam intermediate rotates ~180° around the C3-COO$^-$−Arg267 axis, which results in the *β*-lactam ring of (3*S*,5*R*)-carbapenam moving away from the Tyr191 and Trp202 and toward Val92 in the desaturation process.[28] However, our calculation results indicate that the (3*S*,5*R*)-carbapenam rotates around the C7-keto−Tyr191 axis. Residues Tyr165 and Tyr191 are located within hydrogen-bonding distances to (3*S*,5*R*)-carbapenam, which were not observed in the previous docking model. These hydrogen bonding interactions are necessary for properly positioning (3*S*,5*R*)-carbapenam. In model ^{5}C, the *d*(O−H22) is 4.70 Å, which implies that H22 atom is not accessible to the Fe^{IV}=O/Fe^{III}−OH center. Whereas the energy of model ^{5}D is 1.4 kcal/mol higher than that of ^{5}C, both *d*(O−H3) and *d*(O−H22) are suitable for the desaturation reaction. In addition, in both models ^{5}C and ^{5}D, the *d*(O−H3) is much shorter than the *d*(O−H22), suggesting that the Fe^{IV}=O species prefers to first activate the C3−H3 bond. In model ^{5}E, we attempt to find another possibility for the Fe^{IV}=O species to abstract a hydrogen atom from C2 rather than from C3; however, the optimized structure is energetically quite unfavorable compared with ^{5}C. Thus, model ^{5}D is the most likely one to start the desaturation process. On the basis of model ^{5}D, we explored the CarC-catalyzed desaturation process.

3.5.1. Hydrogen Atom Abstraction.

The optimized geometries of all structures for the CarC-catalyzed desaturation reaction are shown in Figure S10. The desaturation of (3*S*,5*R*)-carbapenam starts with a hydrogen atom abstraction by the Fe^{IV}=O species, which is similar to the epimerization of (3*S*,5*S*)-carbapenam. Previous DFT calculations have proposed that the Fe^{IV}=O species abstracts the hydrogen atom from either C3 or C2 of (3*S*,5*R*)-carbapenam with comparable rate-limiting barriers.[29] However, this result is inherently speculative because the real protein environment was not taken into consideration. Our calculation results clearly indicated that the Fe^{IV}=O species abstracts a hydrogen atom from C3 to form Fe^{III}−OH species and a C3-radical intermediate (^{5}Int5). In ^{5}Int4 (model ^{5}D), the *d*(O−H3) is 2.27 Å, and the Fe−O−H3 angle is 126.6°. Arg267 forms a hydrogen bond to the oxo group of the Fe^{IV}=O species with a distance of 2.11 Å. In addition, Tyr165 and Tyr191 are responsible for properly positioning the (3*S*,5*R*)-carbapenam intermediate by hydrogen-bonding interactions.

The hydrogen atom abstraction barrier is 11.7 kcal/mol, which is much lower than the rate-limiting hydrogen atom abstraction barrier in the epimerization process. This can be ascribed mainly to the shorter *d*(O−H3) as well as more suitable Fe−O−H3 angle compared with ^{5}R′, which cause more effective orbital overlap between the Fe−O and the C3−H3 bonds.

3.5.2. Formation of (5R)-Carbapenem.

After the formation of the C3-radical, the C2−H22 bond is activated by the Fe^{III}−OH species, generating the Fe^{II} ion, water molecule, and final product (5*R*)-carbapenem (P). Although the *d*(O−H22) in ^{5}Int5 seems to be a little long (3.01 Å), the migration of the H3 atom weakens the interaction between the Fe and O atoms, which facilitates the departure of OH from Fe^{III} and activation of the C2−H22 bond. The activation barrier of this step is 5.0 kcal/mol relative to ^{5}Int5.

In ^{5}P, the generated water molecule and Tyr165 form two strong hydrogen bonds with product (5*R*)-carbapenem with distances of 1.51 and 1.68 Å. As can be seen from Figure 9, the H3 atom abstraction is an endothermic process (5.8 kcal/mol), whereas the formation of (5*R*)-carbapenem is found to be remarkably exothermic by −38.0 kcal/mol. The formation of (5*R*)-carbapenem leads to the regeneration of the ferrous resting state of the enzyme.

We also explored the hydroxyl group rebound from the Fe^{III}−OH species to the C3-radical to form the byproduct (3*S*,5*R*)-3-hydroxylcarbapenam (P′). The barrier of OH

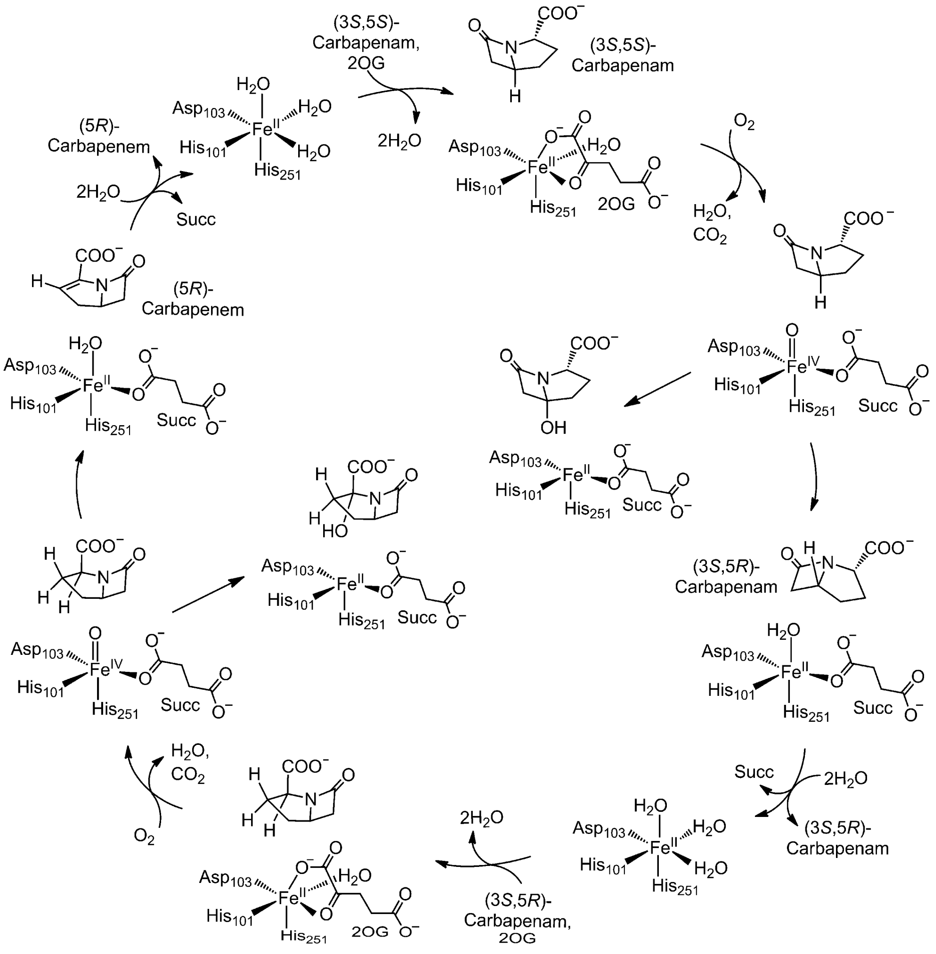

Figure 11. Proposed catalytic cycle of CarC.

rebound is 4.5 kcal/mol relative to ^{5}Int5, which is just slightly lower than that of the formation of (5R)-carbapenem. Energetically, the byproduct ^{5}P′ is −12.0 kcal/mol lower than target product ^{5}P, which is attributed at least in part to the hydrolytic lability of the product. Consequently, the quintet spin pathway gives a mixture of desaturation and hydroxylation products.

Taken together, the calculation results support the previously proposed uncoupled desaturation mechanism, in which no active site residue is involved except $Fe^{IV}{=}O$ species. Although the Tyr165, which acts as a hydrogen donor in epimerization, is not implicated in the desaturation process, it is essential for the binding of the (3S,5R)-carbapenam intermediate. In addition, although the desaturation competes with the substrate hydroxylation, it occurs more efficiently than the epimerization step. Using the (3S,5S)-carbapenam substrate, the predominant products of CarC catalysis are the inverted (3S,5R)-carbapenam and (3S,5R)-5-hydroxylcarbapenam. To obtain the (5R)-carbapenem product, the superior substrate is (3S,5R)-carbapenam for CarC, which is in good agreement with the experimental observations.[28]

3.6. Catalytic Cycle of CarC. On the basis of the experimental observations[28,30] and our calculation results, we propose a complete catalytic cycle of CarC, as shown in Figure 11. In the resting state of CarC, the ferrous ion binds a His-Asp-His facial triad (His101, Asp103, and His251) and three water molecules. Following the binding of substrate (3S,5S)-carbapenam, 2OG, and dioxygen, the oxidative decarboxylation of 2OG yields succinate, CO_2, and $Fe^{IV}{=}O$ species. The whole catalytic cycle involves two rounds of dioxygen activation and $Fe^{IV}{=}O$ formation. The highly reactive $Fe^{IV}{=}O$ species initiates the uncoupled epimerization and desaturation by hydrogen atom abstraction reactions. Despite the competitive substrate hydroxylation, the epimerization and desaturation of (3S,5S)-carbapenam catalyzed by CarC produce the structurally simplest (5R)-carbapenem, which is the key core of various carbapenem drugs.

4. CONCLUSIONS

In this work, we report the first QM/MM studies of the C5-epimerization and C2/3-desaturation mechanisms of CarC. On the basis of the recently reported crystal structure, we analyzed the dioxygen binding site on the iron and found that dioxygen can bind to iron with two different positions: trans to His101 or trans to His251. Both of the binding models are stereochemically and energetically feasible. As such, the obtained iron(IV)−oxo complex from oxidative decarboxylation of 2OG by iron(III)−superoxo has two potential orientations with the oxo group either trans to His101 or trans to His251. The former is energetically unstable, and has no reactivity because the oxo group is far from the substrate. However, it can rapidly isomerize into the latter by the rotation of the oxo group with a low-energy transition state (1.6 kcal/mol). The latter is suggested to be the truly reactive species to initiate the epimerization and desaturation processes. Arg279 plays important roles in regulating the dioxygen binding and assisting the isomerization of Fe^{IV}−oxo species.

Despite the competitive substrate hydroxylation, our studies clearly support the stepwise epimerization and desaturation processes, involving two rounds of dioxygen activation and Fe^{IV}═O formation, which is in agreement with the recent experimental proposal.[28,30] The CarC-catalyzed epimerization reaction includes the rate-limiting H5 atom abstraction by Fe^{IV}═O species (20.4 kcal/mol), inversion of the C5-radical, and reconstitution of an inverted C5−H bond. The calculation results confirmed that Tyr165 is the sole hydrogen donor to reconstitute the C5−H bond. It is suggested that after the epimerization reaction, the generated (3*S*,5*R*)-carbapenam releases from the CarC and then rebinds to the active site with a new orientation. The C2−C3 desaturation reaction occurs without involving any active site residue except the Fe^{IV}═O center. The Fe^{IV}═O species first abstracts the H3 atom, rather than the H2 atom, to form the C3-radical intermediate and Fe^{III}−OH species. Subsequently, the Fe^{III}−OH abstracts the H2 atom, leading to the Fe^{II} ion; water molecule; and final product, (5*R*)-carbapenem. Although the Tyr165 is not involved in the desaturation reaction, it plays an essential role in the binding of (3*S*,5*R*)-carbapenam. In addition, the calculated results indicate that the predominant products for CarC are the inverted (3*S*,5*R*)-carbapenam and (3*S*,5*R*)-5-hydroxyl-carbapenam by using substrate (3*S*,5*S*)-carbapenam. In contrast, if the substrate is (3*S*,5*R*)-carbapenam, CarC can directly give a mixture of (5*R*)-carbapenem and (3*S*,5*R*)-3-hydroxylcarbapenam products. Our studies may provide meaningful insight into the reaction mechanism of CarC, which is helpful in the engineering of carbapenem biosynthesis.

■ ASSOCIATED CONTENT

Ⓢ Supporting Information

The Supporting Information is available free of charge on the ACS Publications website at DOI: 10.1021/acscatal.5b01275.

> RMSDs for the protein backbone atoms along the MD trajectory; superimposition of active sites of QM/MM-optimized geometries of enzyme−substrate complexes; natural orbitals of $^5R'$ and ^{5}Int1; calculated QM/MM energy profiles; optimized geometries of all the structures; spin population for some key atoms, absolute QM/MM single-point energies corrected for dispersion effects and Cartesian coordinates of all the structures (PDF)

■ AUTHOR INFORMATION

Corresponding Author

*E-mail: yongjunliu_1@sdu.edu.cn.

Notes

The authors declare no competing financial interest.

■ ACKNOWLEDGMENTS

This work was supported by the Natural Science Foundation of China (21373125, 21173129).

■ REFERENCES

(1) Bradley, J. S.; Garau, J.; Lode, H.; Rolston, K.V. I.; Wilson, S. E.; Quinn, J. P. *Int. J. Antimicrob. Agents* **1999**, *11*, 93−100.

(2) Goa, K. L.; Noble, S. *Drugs* **2003**, *63*, 913−926.

(3) Edwards, J. R. *J. Antimicrob. Chemother.* **1995**, *36*, 1−17.

(4) Shah, P. M.; Isaacs, R. D. *J. Antimicrob. Chemother.* **2003**, *52*, 538−542.

(5) Paterson, D. L.; DePestel, D. D. *Clin. Infect. Dis.* **2009**, *49*, 291−298.

(6) Papp-Wallace, K. M.; Endimiani, M.; Taracila, M. A.; Bonomo, R. A. *Antimicrob. Agents Chemother.* **2011**, *55*, 4943−4960.

(7) Hamed, R. B.; Gomez-Castellanos, J. R.; Henry, L.; Ducho, C.; McDonough, M. A.; Schofield, C. J. *Nat. Prod. Rep.* **2013**, *30*, 21−107.

(8) Coulthurst, S. J. A.; Barnard, M.; Salmond, G. P. *Nat. Rev. Microbiol.* **2005**, *3*, 295−306.

(9) Chouchani, C.; Marrakchi, R.; El Salabi, A. *Crit. Rev. Microbiol.* **2011**, *37*, 167−177.

(10) Livermore, D. M.; Warner, M.; Mushtaq, S.; Doumith, M.; Zhang, J.; Woodford, N. *Int. J. Antimicrob. Agents* **2011**, *37*, 415−419.

(11) Nordmann, P.; Picazo, J. J.; Mutters, R.; Korten, V.; Quintana, A.; Laeuffer, J. M.; Seak, J. C. H.; Flamm, R. K.; Morrissey, I. *J. Antimicrob. Chemother.* **2011**, *66*, 1070−1078.

(12) Patel, G.; Bonomo, R. A. *Expert Rev. Anti-Infect. Ther.* **2011**, *9*, 555−570.

(13) Kahan, J. S.; Kahan, F. M.; Goegelman, R.; Currie, S. A.; Jackson, M.; Stapley, E. O.; Miller, T. W.; Miller, A. K.; Hendlin, D.; Mochales, S.; Hernandez, S.; Woodruff, H. B.; Birnbaum, J. *J. Antibiot.* **1979**, *32*, 1−12.

(14) Li, R.; Stapon, A.; Blanchfield, J. T.; Townsend, C. A. *J. Am. Chem. Soc.* **2000**, *122*, 9296−9297.

(15) Gerratana, B.; Stapon, A.; Townsend, C. A. *Biochemistry* **2003**, *42*, 7836−7847.

(16) Stapon, A.; Li, R.; Townsend, C. A. *J. Am. Chem. Soc.* **2003**, *125*, 15746−15747.

(17) Bodner, M. J.; Li, R.; Phelan, R. M.; Freeman, M. F.; Moshos, K. A.; Lloyd, E. P.; Townsend, C. A. *ChemBioChem* **2011**, *12*, 2159−2165.

(18) Clifton, I. J.; Doan, L. X.; Sleeman, M. C.; Topf, M.; Suzuki, H.; Wilmouth, R. C.; Schofield, C. J. *J. Biol. Chem.* **2003**, *278*, 20843−20850.

(19) Pavel, E. G.; Zhou, J.; Busby, R. W.; Gunsior, M.; Townsend, C. A.; Solomon, E. I. *J. Am. Chem. Soc.* **1998**, *120*, 743−753.

(20) Zhou, J.; Kelly, W. L.; Bachmann, B. O.; Gunsior, M.; Townsend, C. A.; Solomon, E. I. *J. Am. Chem. Soc.* **2001**, *123*, 7388−7398.

(21) Borowski, T.; Bassan, A.; Siegbahn, P. E. M. *Chem. - Eur. J.* **2004**, *10*, 1031−1041.

(22) Grzyska, P. K.; Appelman, E. H.; Hausinger, R. P.; Proshlyakov, D. A. *Proc. Natl. Acad. Sci. U. S. A.* **2010**, *107*, 3982−3987.

(23) Krebs, C.; Galonić Fujimori, D.; Walsh, C. T.; Bollinger, J. M., Jr. *Acc. Chem. Res.* **2007**, *40*, 484−492.

(24) Ghosh, A. *J. Inorg. Biochem.* **2006**, *100*, 419−420.

(25) Hausinger, R. P. *Crit. Rev. Biochem. Mol. Biol.* **2004**, *39*, 21−68.

(26) Stapon, A.; Li, R.; Townsend, C. A. *J. Am. Chem. Soc.* **2003**, *125*, 8486−8493.

(27) Phelan, R. M.; DiPardo, B. J.; Townsend, C. A. *ACS Chem. Biol.* **2012**, *7*, 835−840.

(28) Phelan, R. M.; Townsend, C. A. *J. Am. Chem. Soc.* **2013**, *135*, 7496−7502.

(29) Borowski, T.; Broclawik, E.; Schofield, C. J.; Siegbahn, P. E. *J. Comput. Chem.* **2006**, *27*, 740−748.

(30) Chang, W. C.; Guo, Y.; Wang, C.; Butch, S. E.; Rosenzweig, A. C.; Boal, A. K.; Krebs, C.; Bollinger, J. M., Jr. *Science* **2014**, *343*, 1140−1144.

(31) Hangasky, J. A.; Gandhi, H.; Valliere, M. A.; Ostrom, N. E.; Knapp, M. J. *Biochemistry* **2014**, *53*, 8077−8084.

(32) Zhang, Z.; Ren, J.; Stammers, D. K.; Baldwin, J. E.; Harlos, K.; Schofield, C. J. *Nat. Struct. Biol.* **2000**, *7*, 127−133.

(33) Topf, M.; Sandala, G. M.; Smith, D. M.; Schofield, C. J.; Easton, C. J.; Radom, L. *J. Am. Chem. Soc.* **2004**, *126*, 9932−9933.

(34) Shaik, S.; Kumar, D.; de Visser, S. P.; Altun, A.; Thiel, W. *Chem. Rev.* **2005**, *105*, 2279−2328.

(35) Shaik, S.; Cohen, S.; Wang, Y.; Chen, H.; Kumar, D.; Thiel, W. *Chem. Rev.* **2010**, *110*, 949−1017.

(36) Wang, B.; Usharani, D.; Li, C.; Shaik, S. *J. Am. Chem. Soc.* **2014**, *136*, 13895−13901.

(37) Quesne, M. G.; Latifi, R.; Gonzalez-Ovalle, L. E.; Kumar, D.; de Visser, S. P. *Chem. - Eur. J.* **2014**, *20*, 435−446.

(38) Saura, P.; Suardíaz, R.; Masgrau, L.; Lluch, J. M.; González-Lafont, À. *ACS Catal.* **2014**, *4*, 4351−4363.

(39) Olsson, M. H.; Søndergard, C. R.; Rostkowski, M.; Jensen, J. H. *J. Chem. Theory Comput.* **2011**, *7*, 525−537.

(40) Humphrey, W.; Dalke, A.; Schulten, K. *J. Mol. Graphics* **1996**, *14*, 33−38.

(41) Brooks, B. R.; Bruccoleri, R. E.; Olafson, B. D.; States, D. J.; Swaminathan, S.; Karplus, M. *J. Comput. Chem.* **1983**, *4*, 187−217.

(42) MacKerell, A. D., Jr.; Bashford, D.; Bellott, M.; Dunbrack, R. L., Jr.; Evanseck, J. D.; Field, M. J.; Fischer, S.; Gao, J.; Guo, H.; Ha, S.; Joseph-McCarthy, D.; Kuchnir, L.; Kuczera, K.; Lau, F. T. K.; Mattos, C.; Michnick, S.; Ngo, T.; Nguyen, D. T.; Prodhom, B.; Reiher, W. E., III; Roux, B.; Schlenkrich, M.; Smith, J. C.; Stote, R.; Straub, J.; Watanabe, M.; Wiorkiewicz-Kuczera, J.; Yin, D.; Karplus, M. *J. Phys. Chem. B* **1998**, *102*, 3586−3616.

(43) Sherwood, P.; de Vries, A. H.; Guest, M. F.; Schreckenbach, G.; Catlow, C. R. A.; French, S. A.; Sokol, A. A.; Bromley, S. T.; Thiel, W.; Turner, A. J.; Billeter, S.; Terstegen, F.; Thiel, S.; Kendrick, J.; Rogers, S. C.; Casci, J.; Watson, M.; King, F.; Karlsen, E.; Sjovoll, M.; Fahmi, A.; Schafer, A.; Lennartz, C. *J. Mol. Struct.: THEOCHEM* **2003**, *632*, 1−28.

(44) Ahlrichs, R.; Bär, M.; Häser, M.; Horn, H.; Kölmel, C. *Chem. Phys. Lett.* **1989**, *162*, 165−169.

(45) Smith, W.; Forester, T. R. *J. Mol. Graphics* **1996**, *14*, 136−141.

(46) Bakowies, D.; Thiel, W. *J. Phys. Chem.* **1996**, *100*, 10580−10594.

(47) de Vries, A. H.; Sherwood, P.; Collins, S. J.; Rigby, A. M.; Rigutto, M.; Kramer, G. J. *J. Phys. Chem. B* **1999**, *103*, 6133−6141.

(48) Becke, A. D. *J. Chem. Phys.* **1993**, *98*, 5648−5652.

(49) Wachters, A. J. H. *J. Chem. Phys.* **1970**, *52*, 1033−1036.

(50) Chen, H.; Ikeda-Saito, M.; Shaik, S. *J. Am. Chem. Soc.* **2008**, *130*, 14778−14790.

(51) Billeter, S. R.; Turner, A. J.; Thiel, W. *Phys. Chem. Chem. Phys.* **2000**, *2*, 2177−2186.

(52) Nocedal, J. *Math. Comput.* **1980**, *35*, 773−782.

(53) Liu, D. C.; Nocedal, J. *Math. Prog.* **1989**, *45*, 503−528.

(54) Banerjee, A.; Adams, N.; Simons, J.; Shepard, R. *J. Phys. Chem.* **1985**, *89*, 52−57.

(55) Grimme, S.; Antony, J.; Ehrlich, S.; Krieg, H. *J. Chem. Phys.* **2010**, *132*, 154104.

(56) Lonsdale, R.; Harvey, J. N.; Mulholland, A. J. *J. Phys. Chem. Lett.* **2010**, *1*, 3232−3237.

(57) Borowski, T.; Noack, H.; Radon, M.; Zych, K.; Siegbahn, P. E. M. *J. Am. Chem. Soc.* **2010**, *132*, 12887−12898.

(58) Ma, G.; Cheng, N.; Su, H.; Liu, Y. *RSC Adv.* **2015**, *5*, 7781−7788.

(59) Lonsdale, R.; Harvey, J. N.; Mulholland, A. J. *J. Phys. Chem. B* **2010**, *114*, 1156−1162.

(60) Claeyssens, F.; Ranaghan, K. E.; Manby, F. R.; Harvey, J. N.; Mulholland, A. J. *Chem. Commun.* **2005**, 5068−5070.

(61) Ye, S.; Neese, F. *Proc. Natl. Acad. Sci. U. S. A.* **2011**, *108*, 1228−1233.

(62) Godfrey, E.; Porro, C. S.; de Visser, S. P. *J. Phys. Chem. A* **2008**, *112*, 2464−2468.

(63) Shaik, S.; Chen, H.; Janardanan, D. *Nat. Chem.* **2011**, *3*, 19−27.

(64) Neidig, M. L.; Decker, A.; Choroba, O. W.; Huang, F.; Kavana, M.; Moran, G. R.; Spencer, J. B.; Solomon, E. I. *Proc. Natl. Acad. Sci. U. S. A.* **2006**, *103*, 12966−12973.

(65) Geng, C.; Ye, S.; Neese, F. *Angew. Chem.* **2010**, *122*, 5853−5856.

(66) Kumar, D.; Hirao, H.; Que, L., Jr.; Shaik, S. *J. Am. Chem. Soc.* **2005**, *127*, 8026−8027.

(67) de Visser, S. P. *J. Am. Chem. Soc.* **2006**, *128*, 15809−15818.

(68) Ji, L.; Faponle, A. S.; Quesne, M. G.; Sainna, M. A.; Zhang, J.; Franke, A.; Kumar, D.; van Eldik, R.; Liu, W.; de Visser, S. P. *Chem. - Eur. J.* **2015**, *21*, 9083−9092.